SCIENCE CHINA
Earth Sciences

• RESEARCH PAPER •

March 2017 Vol.60 No.3: 478–490
doi: 10.1007/s11430-015-0271-4

Handling non-linearity in radar data assimilation using the non-linear least squares enhanced POD-4DVar

ZHANG Bin[1,2], TIAN XiangJun[1,3*], ZHANG LiFeng[2] & SUN JianHua[3,4]

[1] *International Center for Climate and Environment Sciences (ICCES), Institute of Atmospheric Physics, Chinese Academy of Sciences, Beijing 100029, China;*
[2] *College of Meteorology and Oceanography, PLA University of Science and Technology, Nanjing 211101, China;*
[3] *Collaborative Innovation Center on Forecast and Evaluation of Meteorological Disasters, Nanjing University of Information Science & Technology, Nanjing 210044, China;*
[4] *Ley Laboratory of Cloud-Precipitation Physics and Severe Storms (LACS), Institute of Atmospheric Physics, Chinese Academy of Sciences, Beijing 100029, China*

Received September 27, 2016; accepted December 9, 2016; published online January 24, 2017

Abstract The Proper Orthogonal Decomposition (POD)-based ensemble four-dimensional variational (4DVar) assimilation method (POD4DEnVar) was proposed to combine the strengths of EnKF (i.e., the ensemble Kalman filter) and 4DVar assimilation methods. Recently, a POD4DEnVar-based radar data assimilation scheme (PRAS) was built and its effectiveness was demonstrated. POD4DEnVar is based on the assumption of a linear relationship between the model perturbations (MPs) and the observation perturbations (OPs); however, this assumption is likely to be destroyed by the highly non-linear forecast model or observation operator. To address this issue, using the Gauss-Newton iterative method, the nonlinear least squares enhanced POD4DEnVar algorithm (referred to as NLS-4DVar) was proposed. Naturally, the PRAS was upgraded to form the NLS-4DVar-based radar data assimilation scheme (NRAS). To evaluate the performance of NRAS against PRAS, observing system simulation experiments (OSSEs) were conducted to assimilate reflectivity and radial velocity individually, with one, two, and three iterations. The results demonstrated that the NRAS outperformed PRAS in improving the initial condition and the forecasting of model variables and rainfall. The NRAS, with a smaller number of iterations, can yield a convergent result. In contrast to the situation when assimilating radial velocity, the advantages of NRAS over PRAS were more obvious when assimilating reflectivity.

Keywords Data assimilation, Non-linearity, Gauss-Newton, NRAS, PRAS, Radar reflectivity, Radial velocity

Citation: Zhang B, Tian X J, Zhang L F, Sun J H. 2017. Handling non-linearity in radar data assimilation using the non-linear least squares enhanced POD-4DVar. Science China Earth Sciences, 60: 478–490, doi: 10.1007/s11430-015-0271-4

1. Introduction

Doppler radar observations have high temporal and spatial resolutions, and the radial velocity and reflectivity obtained from Doppler radars contain important convective scale information on the wind and hydrometeors (Weng et al., 2011; Zhang, 2011; Zhang et al., 2011). As high-resolution simulations are developed for numerical weather prediction (NWP), assimilating radar data is essential for improving the capacity of NWP (Choi et al., 2013).

There are two main methods to effectively assimilate radar data: the variational and sequential methods. In variational methods, three-dimensional variational (3DVar) analysis was first used to assimilate radar data with a 3DVar system, Doppler radar data were assimilated successfully to initiate the convective system and improve short-range rainfall forecasts (Gao et al., 2004; Hu et al., 2006a, 2006b; Xiao et al., 2005, 2007; Xiao and Sun, 2007; Sugimoto et al., 2009; Kain

*Corresponding author(email: tianxj@mail.iap.ac.cn)

et al., 2010), and the Weather Research and Forecast (WRF) 3DVar radar data assimilation system was also implemented operationally in the Korea Meteorological Administration (KMA; Xiao et al., 2008). Recently, Wang et al. (2013a) further upgraded the 3DVar radar data assimilation scheme by adding the assimilation of in-cloud humidity. Although 3DVar can effectively assimilate radar data, it neglects the time tendency of atmospheric flow and cannot assimilate radar data distributed dynamically over time (Sun and Wang, 2013). Additionally, 3DVar does not include the effects of "errors of the day", the background error covariance is assumed to be static, homogeneous, and isotropic (Courtier, 2007; Parrish and Derber, 1992; Lorenc, 2003), which is always inappropriate in the analysis of fast-evolving convective scale systems.

While the four-dimensional variational (4DVar) technique uses a forecast model as a constraint and can assimilate asynoptic observations in time, the time tendency terms are also included (Sun and Wang, 2013). In addition, 4DVar can implicitly evolve background error covariance over an assimilation window and so reflect the flow-dependent nature of the analysis increments (Huang et al., 2009). For radar data assimilation, Sun and Wang (2013) compared the WRF 4DVar system with its corresponding 3DVar system and an enhanced 3DVar system (Wang H L et al., 2013a). The results indicated that 4DVar substantially improves the quantitative precipitation forecast (QPF) skill over the standard 3DVar and the enhanced 3DVar. Recently, assimilating radar data with 4DVar has shown the potential for improving the QPF of mesoscale convective systems (Kawabata et al., 2007, 2011; Wang et al., 2013b; Sun and Wang, 2013; Choi et al., 2013). However, the traditional 4DVar method is an adjoint-based method, which faces a range of challenges arising from coding, maintaining, and updating the adjoint model of the forecast model. In addition, the background error covariance at the beginning of the assimilation window is assumed to be static for 4DVar (Kleist and Ide, 2015a, 2015b), which leads to its poor assimilation performance (Beck and Ehrendorfer, 2005; Cheng et al., 2010; Fairbairn et al., 2014).

For sequential methods, since the ensemble Kalman filter (EnKF) technique was introduced by Evensen (1994), it has received much attention due to its simple conceptual formulation and relative ease of implementation (Evensen, 2003). It uses ensemble forecasts to estimate flow-dependent background error covariance, including cross-covariances among variables, and can effectively extract information contained in radar data, such that many encouraging results have been obtained from EnKF-based radar data assimilation (e.g., Snyder and Zhang, 2003; Dowell et al, 2004; Tong and Xue, 2005; Aksoy et al., 2009, 2010; Jung et al., 2008, 2010; Xue et al., 2010; Snook et al., 2011; Weng and Zhang, 2012; Munsell and Zhang, 2014). However, EnKF lacks the temporal smoothness constraint and evolution of nonlinearities for forecast errors over the assimilation window in 4DVar (Caya et al., 2005).

Generally, 4DVar and EnKF can both assimilate radar data well due to their respective advantages (Caya et al., 2005). In an attempt to combine the strengths of these two main assimilation methods, so-called 4DEnVar methods (Lorenc, 2003, 2013; Lorenc et al., 2015; Desroziers et al., 2014; Fairbairn et al., 2014; Poterjoy and Zhang, 2015) have been proposed (e.g., Qiu et al., 2007; Liu et al., 2008, 2009; Tian et al., 2008, 2011; Wang et al., 2010). In 4DEnVar, the 4D ensemble of model trajectories is used to calculate perturbations and hence evolve background error covariance flow-dependently instead of using the tangent linear and adjoint models in 4DVar (Fairbairn et al., 2014; Buehner et al., 2013), and the localization of background error covariance in observation space in comparison to EnKF is avoided, while highly parallel computing can be easily performed (Desroziers et al., 2014). Recently, many applications based on these 4DEnVar methods have shown its potential in different fields (e.g., Wang et al., 2010; Tian et al., 2014; Zhang et al., 2015). Of these, the proper orthogonal decomposition (POD)-based ensemble 4DVar assimilation method (referred to as POD4DEnVar, Tian et al., 2008, 2011) was proposed based on the POD and ensemble forecast techniques. For POD4DEnVar, the POD transformation is conducted in the observation perturbation (OP) space rather than in the model perturbation (MP) space, and the MPs are transformed in accordance with the POD transformation to the OP space. Thus, the computational cost can be substantially reduced (Tian et al., 2011). Meanwhile, the transformed MPs could guarantee the orthogonality (and thus independence) of their corresponding OPs (Tian et al., 2011), which is more conducive to obtaining good assimilation results. Furthermore, Zhang et al. (2015) used this approach to build a POD4DEnVar-based radar data assimilation scheme (PRAS), which significantly improved the accuracy of analysis fields and rainfall forecast. However, POD4DEnVar assumes a linear relationship between the MPs and OPs (Tian and Feng, 2015). As Tian and Feng (2015) discussed, such a linear assumption is inevitably challenged when the forecast model or observation operator is strongly non-linear. For example, the length of the assimilation window in PRAS has to be chosen carefully to guarantee the linear assumption between the MPs and OPs (Zhang et al., 2015). Nevertheless, PRAS inevitably suffers from the linear assumption. To solve the nonlinear problems in data assimilation, the incremental 4D-Var (Courtier et al., 1994) uses outer loops to update the nonlinear evolution of the trajectory, while the incremental cost function is minimized in the inner loops (Andersson et al., 2005; Huang et al., 2009). In EnKF, to solve the nonlinear problems, Kalnay and Yang (2008, 2010) used the no-cost smoothing and 'running in place' methods, and the observations were assimilated more than once during spin-up to maximize the initial extrac-

tion of information (Kalnay and Yang, 2008, 2010; Yang et al., 2012; Wang S Z et al., 2013). Sakov et al. (2012) proposed an iterative EnKF, while Bocquet and Sakov (2014) proposed an iterative ensemble Kalman smoother, in which the Gauss-Newton schemes were used to minimize the cost function iteratively. Similarly, with the Gauss-Newton iterative method, Tian and Feng (2015) proposed a nonlinear least squares enhanced POD-4DVar algorithm (NLS-4DVar) to solve the nonlinear problems in POD4DEnVar. The results demonstrated that NLS-4DVar performed moderately better than POD4DEnVar for highly non-linear cases.

Because of the advantages of NLS-4DVar over the POD4DEnVar, naturally, we further upgraded PRAS to a new radar data assimilation scheme based on the proposed NLS-4DVar approach (NRAS). In this study, observing system simulation experiments (OSSEs) were designed to evaluate the assimilation performance of NRAS against PRAS.

2. Methodology

2.1 Formulation of the NLS-4DVar

As an enhanced version of the POD4DEnVar (Tian et al., 2008, 2011), NLS-4DVar also prepares an ensemble of initial fields ($\boldsymbol{x}_j$, j=1, ..., N, N is the number of ensemble members) to represent the uncertainty of the background field $\boldsymbol{x}_b$ at an initial time of t_1. Further, NLS-4DVar assumes the analysis increment $\boldsymbol{x}'_a$ linearly embeds in the MPs' space ($\boldsymbol{x}'_j = \boldsymbol{x}'_j - \boldsymbol{x}'_b j$=1, ..., N); then, $\boldsymbol{x}'_a$ can be expressed as follows:

$$x'_a = \boldsymbol{P}_x \boldsymbol{\beta}, \tag{1}$$

where $\boldsymbol{P}_x = (\boldsymbol{x}'_1, \boldsymbol{x}'_2, \cdots, \boldsymbol{x}'_N)$, $\boldsymbol{\beta} = (\beta_1, \beta_2, \cdots, \beta_N)^{\mathrm{T}}$.

Substituting eq. (1) and the ensemble background error covariance $\boldsymbol{B}$=$\boldsymbol{P}_x\boldsymbol{P}_x^{\mathrm{T}}$/($N$−1) (Evensen, 2004) into the following incremental form of the 4DVar cost function

$$\begin{aligned} J(\boldsymbol{x}') = & \frac{1}{2}(\boldsymbol{x}')^{\mathrm{T}}\boldsymbol{B}^{-1}(\boldsymbol{x}') \\ & + \frac{1}{2}\sum_{k=1}^{s}\left[H_k M_{t_1\to t_k}(\boldsymbol{x}_b + \boldsymbol{x}') - \boldsymbol{y}_k^{\mathrm{obs}}\right]^{\mathrm{T}}\boldsymbol{R}_k^{-1} \\ & \times\left[H_k M_{t_1\to t_k}(\boldsymbol{x}_b + \boldsymbol{x}') - \boldsymbol{y}_k^{\mathrm{obs}}\right], \end{aligned} \tag{2}$$

the control variable becomes $\boldsymbol{\beta}$=(β_1, β_2, ..., β_N)$^{\mathrm{T}}$ instead of x' as follows:

$$\begin{aligned} J(\boldsymbol{\beta}) = & \frac{1}{2}(N-1)\boldsymbol{\beta}^{\mathrm{T}}\boldsymbol{\beta} \\ & + \frac{1}{2}\sum_{k=1}^{s}\left[H_k M_{t_1\to t_k}(\boldsymbol{x}_b + \boldsymbol{P}_x\boldsymbol{\beta}) - \boldsymbol{y}_k^{\mathrm{obs}}\right]^{\mathrm{T}}\boldsymbol{R}_k^{-1} \\ & \times\left[H_k M_{t_1\to t_k}(\boldsymbol{x}_b + \boldsymbol{P}_x\boldsymbol{\beta}) - \boldsymbol{y}_k^{\mathrm{obs}}\right], \end{aligned} \tag{3}$$

Here, T and b represent the matrix transpose and the background field, respectively. t_k indicates the kth observation time, s is the total observation time steps in the assimilation window. H_k, $M_{t_1\to t_k}$, $\boldsymbol{B}$, and $\boldsymbol{R}_k$ represent the observation operator, the forecast model, the background error covariance, and the observation error covariance, respectively.

Through the appropriate mathematical calculations (see Tian and Feng (2015) for more details), eq. (3) can be rewritten as the following nonlinear least squares formulation:

$$J(\boldsymbol{\beta}) = \frac{1}{2}\boldsymbol{Q}(\boldsymbol{\beta})^{\mathrm{T}}Q(\boldsymbol{\beta}), \tag{4}$$

where

$$\boldsymbol{Q}(\boldsymbol{\beta}) = \begin{pmatrix} \boldsymbol{R}_1^{-1/2}\left[L'_1(\boldsymbol{P}_x\boldsymbol{\beta}) - (\boldsymbol{y}_1^{\mathrm{obs}})'\right] \\ \vdots \\ \boldsymbol{R}_s^{-1/2}\left[L'_s(\boldsymbol{P}_x\boldsymbol{\beta}) - (\boldsymbol{y}_s^{\mathrm{obs}})'\right] \\ \sqrt{N-1}\,\boldsymbol{\beta} \end{pmatrix}, \tag{5}$$

$$\boldsymbol{R}_k = \boldsymbol{R}_k^{1/2}\left(\boldsymbol{R}_k^{1/2}\right)^{\mathrm{T}}, \tag{6}$$

$$L'_k(\boldsymbol{x}') = H_k M_{t_1\to t_k}(\boldsymbol{x}_b + \boldsymbol{x}') - H_k M_{t_1\to t_k}(\boldsymbol{x}_b), \tag{7}$$

$$(\boldsymbol{y}_k^{\mathrm{obs}})' = \boldsymbol{y}_k^{\mathrm{obs}} - H_k M_{t_1\to t_k}(\boldsymbol{x}_b). \tag{8}$$

Therefore, we can obtain the iterative NLS-4DVar analysis solution $x_a'^{,i+1}$ (i=1, 2, ..., $i_{\max}$), $i_{\max}$ is the maximum iteration number, the maximum iteration number is determined when the value of the 4DVar cost function is no longer reduced) after the localization process (Tian and Feng, 2015), as follows:

$$\begin{aligned} x_a'^{,i+1} = & x_a'^{,i} + \left(\boldsymbol{\mu}\circ\boldsymbol{P}_x\hat{\boldsymbol{P}}_y\right)L'\left(\boldsymbol{x}_a'^{,i}\right) \\ & + \left(\boldsymbol{\mu}\circ\boldsymbol{P}_x\widetilde{\boldsymbol{P}}_y\right)\left[(\boldsymbol{y}^{\mathrm{obs}})' - L'\left(\boldsymbol{x}_a'^{,i}\right)\right], \end{aligned} \tag{9}$$

where $\boldsymbol{\mu}\circ\boldsymbol{P}_x\hat{\boldsymbol{P}}_y$ stands for the Schür product of matrices $\boldsymbol{\mu}$ and $\boldsymbol{P}_x\hat{\boldsymbol{P}}_y$ of the same dimension, $\boldsymbol{\mu}\circ\boldsymbol{P}_x\widetilde{\boldsymbol{P}}_y$ stands for the Schür product of matrices $\boldsymbol{\mu}$ and $\boldsymbol{P}_x\widetilde{\boldsymbol{P}}_y$ of the same dimension.

The elements of the matrix $\boldsymbol{\mu}$ can be calculated according to the formula:

$$\mu_{i,j} = C_0(d_{h,i,j}/d_{h,0})\cdot C_0(d_{v,i,j}/d_{v,0}), \tag{10}$$

where the filtering function C_0 is defined by (Gaspari and Cohn, 1999), below:

$$C_0(r) = \begin{cases} -\frac{1}{4}r^5 + \frac{1}{2}r^4 + \frac{5}{8}r^3 - \frac{5}{3}r^2 + 1, & 0 \le r \le 1 \\ \frac{1}{12}r^5 - \frac{1}{2}r^4 + \frac{5}{8}r^3 + \frac{5}{3}r^2 - 5r + 4 - \frac{2}{3}r^{-1}, & 1 < r \le 2 \\ 0, & 2 < r \end{cases} \tag{11}$$

$d_{h,i,j}$ and $d_{v,i,j}$ represent the horizontal distance and vertical distance between the observation point and model grid point;

$d_{h,0}$ and $d_{v,0}$ are the horizontal and vertical localization radii.

$$(\boldsymbol{y}^{\text{obs}})' = \begin{bmatrix} (\boldsymbol{y}_1^{\text{obs}})' \\ (\boldsymbol{y}_2^{\text{obs}})' \\ \vdots \\ (\boldsymbol{y}_s^{\text{obs}}) \end{bmatrix}, \tag{12}$$

$$\hat{\boldsymbol{P}}_y = -\left[(\boldsymbol{P}_y)^{\mathrm{T}}\boldsymbol{R}^{-1}(\boldsymbol{P}_y) + (N-1)\boldsymbol{I}\right]^{-1}(N-1) \times\left[(\boldsymbol{P}_y)^{\mathrm{T}}\boldsymbol{P}_y\right]^{-1}(\boldsymbol{P}_y)^{\mathrm{T}}, \tag{13}$$

$$\widetilde{\boldsymbol{P}}_y = [(\boldsymbol{P}_y)^{\mathrm{T}}\boldsymbol{R}^{-1}(\boldsymbol{P}_y) + (N-1)\boldsymbol{I}]^{-1}(\boldsymbol{P}_y)^{\mathrm{T}}\boldsymbol{R}^{-1}, \tag{14}$$

where

$$\boldsymbol{P}_y = (\boldsymbol{y}'_1, \boldsymbol{y}'_2, \cdots, \boldsymbol{y}'_N). \tag{15}$$

$\boldsymbol{P}_y$ in eq. (15) is referred to as OPs

$$\boldsymbol{y}'_i = \boldsymbol{L}'(\boldsymbol{x}'_i), \tag{16}$$

$$\boldsymbol{L}' = \begin{pmatrix} L'_1 \\ L'_2 \\ \vdots \\ L'_s \end{pmatrix}, \tag{17}$$

$$\text{and } \boldsymbol{R} = \begin{bmatrix} \boldsymbol{R}_1 & 0 & \cdots & 0 \\ 0 & \boldsymbol{R}_2 & \cdots & 0 \\ \vdots & \vdots & \ddots & \vdots \\ 0 & 0 & \cdots & \boldsymbol{R}_s \end{bmatrix}. \tag{18}$$

Generally, the NLS-4DVar is similar to the incremental 4D-Var framework (Courtier et al., 1994). As discussed in Tian and Feng (2015), the non-linear forecast model and the non-linear observation operator are used to update $L'_k(\boldsymbol{x}'^{,i}_a)$, which is similar to the outer loops in the incremental 4D-Var framework. Once $L'_k(\boldsymbol{x}'^{,i}_a)$ is updated, $\boldsymbol{x}'^{,i}_a$ is then updated according to eq. (5). However, the NLS-4DVar does not require the inner loops in the incremental 4D-Var. Since the value of $L'_k(\boldsymbol{x}'^{,i}_a)$ is calculated using the non-linear forecast model and the non-linear observation operator directly, the non-linearity of the original cost function is largely guaranteed. Correspondingly, NLS-4DVar promises to handle the nonlinear data assimilation.

Note that the POD4DEnVar analysis solution is only the first iteration (i.e., $i_{\max}$=1) of the proposed NLS-4DVar sequence (Tian and Feng, 2015). In addition, if the forecast model $M_{t_1\to t_k}$ and observation operator H_k are linear, the NLS-4DVar is equivalent to the POD4DEnVar (Tian and Feng, 2015).

2.2 Observation operator for the NRAS

According to Sun and Crook (1997, 1998), the observation operators for the radial velocity V_r and the reflectivity Z are as follows:

$$V_r = u\frac{x-x_r}{r} + v\frac{y-y_r}{r} + (w - V_{Tm})\frac{z-z_r}{r}, \tag{19}$$

$$Z = 43.1 + 17.5\log(\rho q_r), \tag{20}$$

where (u, v, w) are the zonal wind, meridional wind, and vertical velocity, respectively, the variable r is the distance between the observation location (x, y, z) and the radar location (x_r, y_r, z_r). V_{Tm}, ρ, and q_r represent the mass-weighted terminal velocity of the precipitation, air density, and the rainwater mixing ratio. V_{Tm} and the correction factor a are calculated as follows:

$$V_{Tm} = 5.40aq_r^{0.125}. \tag{21}$$

$$a = \left(\frac{P_0}{\overline{P}}\right)^{0.4}, \tag{22}$$

where $\overline{P}$ and P_0 are the base state pressure and the pressure at the ground surface.

Based on the NLS-4DVar method, the radial velocity and the reflectivity observation operators are introduced, and then NRAS can be formed. In contrast to NRAS, the PRAS is based on the POD4DEnVar, and the solution of PRAS is equivalent to the first iteration solution of the NRAS.

For the NRAS and the PRAS, the zonal wind, the meridional wind, the vertical velocity, the perturbation potential temperature, the perturbation pressure, the water vapor mixing ratio, and the rainwater mixing ratio are control variables.

3. Observing system simulation experiments (OSSEs)

By using OSSEs, a data assimilation system can be investigated comprehensively (Wang et al., 2008; Liu et al., 2009). The OSSEs were designed to evaluate the assimilation performance of the NRAS against the PRAS.

3.1 Description of the experiments

The WRF model was the forecast model used in the OSSEs. In the WRF model, the grid spacing is 6 km with a grid mesh of 400 × 400 in the horizontal direction, and 27 layers in the vertical direction. The Rapid Radiative Transfer Model (RRTM) long-wave radiation scheme, Dudhia shortwave radiation scheme, Yonsei University (YSU) planetary boundary layer (PBL) scheme, WRF single-moment six-classes microphysics (WSM6) scheme, and Noah land surface model (LSM) land scheme were chosen, with the cumulus parameterization scheme excluded.

Because the reflectivity observation operator is non-linear, while the radial velocity observation operator is linear, to clearly investigate the assimilation performance of the NRAS against the PRAS for different radar data, reflectivity and radial velocity were assimilated individually in the experiments. According to Wang et al. (2012) and Zhang et al.

(2015), a 1-hour assimilation window is appropriate and was therefore used here. Because radar data is updated every six minutes in China, the radar data over the assimilation window were assimilated every six minutes.

In the OSSEs, the assumed "true" atmospheric state was initially produced as a reference. To remove the influence of the spin-up, the "true" atmospheric state was initiated from six hours prior to the time of analysis at 0000 UTC 08 July 2010 with 1° × 1° National Centers for Environmental Prediction (NCEP) Final (FNL) Global Tropospheric Analyses. Then the simulated radar observations at the site of the real observations (Wuhan station) were sampled from the assumed "true" atmospheric state. Wuhan radar station is located in Hubei Province (114.38°E, 30.52°N) at an altitude of 135.7 m, and has nine elevation scans, with elevation angles of 0.5°, 1.5°, 2.4°, 3.4°, 4.3°, 6.0°, 9.9°, 14.6°, and 19.5°. The radar observation errors were assumed to be additive, unbiased, and Gaussian. The standard deviations of radial velocity and reflectivity observations were 1 m s^{-1} and 1 dBZ, respectively. A CTL experiment was then conducted to obtain a sizeable different background field from the "true" atmospheric state. The background field was initiated 12 hours prior to the time of analysis with the NCEP FNL data. The MPs ($\boldsymbol{x}'_1, \boldsymbol{x}'_2, \cdots, \boldsymbol{x}'_N$) and OPs ($\boldsymbol{y}'_1, \boldsymbol{y}'_2, \cdots, \boldsymbol{y}'_N$)were formed as in Zhang et al. (2015), with two sampling runs conducted, which were then used to form the ensemble samples using a 4D moving sampling strategy (Wang et al., 2010; Tian et al., 2014).

Once the preparations described above were completed, the OSSEs was conducted to investigate the performance of the NRAS in comparison to the PRAS. Three groups of experiments were designed for assimilating reflectivity (radial velocity), and are referred to as NLS1-R (NLS1-V), NLS2-R (NLS2-V), and NLS3-R (NLS3-V). For the NLS1-R (NLS1-V) experiment, the NRAS conducted only one iteration (i.e., i_{max}=1) to assimilate reflectivity (radial velocity), in which the NRAS was equivalent to the PRAS. For NLS2-R (NLS2-V) and NLS3-R (NLS3-V), the NRAS conducted two or three iterations (i.e., i_{max}=2 or i_{max}=3).

3.2 Effects of radar data assimilation by the NRAS on model initialization

Because the aim of the PRAS and the NRAS is to improve the accuracy of the initial condition, the analysis field at the time of analysis was first compared with the "true" atmospheric state to evaluate the assimilation performance of the NRAS against the PRAS.

First, the radar reflectivity on the eighth model level (σ=0.85 approximately 850 hPa) was compared, as shown in Figures 1 and 2. Figure 1(a) shows the "true" reflectivity, with strong reflectivity in the area of 29°–31°N, 115°–117.5°E. Compared with the "true" reflectivity, the background reflectivity from the control (CTL) experiment (Figure 1(b)) generally reproduced a similar pattern, but there were obvious differences. For example, the CTL experiment failed to simulate the reflectivity between Hubei and Anhui provinces, which corresponded to the gap in the area of 30°–31°N, 115°–116°E (black rectangle) in Figure 1(b).

The simulated reflectivity at the eighth model level in the assimilation experiments is shown in Figure 2. Compared with Figure 1(b), the simulated reflectivity (Figure 2a–c) after assimilating reflectivity was substantially improved, especially in the area of 30°–31°N, 115°–116°E (black rectangle). In the area of 30°–31°N, 115°–116°E (black rectangle), the northern reflectivity was weakened and the southern reflectivity was intensified, which were closer to the "truth" (Figure 1a). This demonstrated that the NRAS can effectively assimilate reflectivity. Compared with NLS1-R (Figure 2a), NLS2-R (Figure 2b) further improved the simulated reflectivity in the area of 30°–31°N, 115°–116°E, which indicated that the NRAS with two iterations outperformed PRAS in assimilating reflectivity. NLS3-R produced a further improvement over NLS2-R. The result indicated the NRAS can grad-

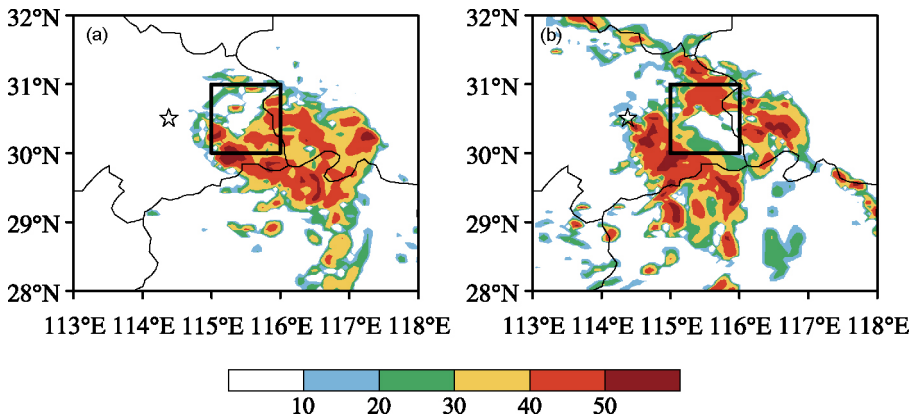

Figure 1 The radar reflectivity (dBZ) at the eighth model level at the time of analysis for (a) the "truth" and (b) the CTL experiment. The black star represents the location of the Doppler radar in Wuhan.

ually improve the simulated reflectivity by increasing the iterations. Further improvements in NLS3-R became fewer, which indicated that the NRAS with two iterations could yield a convergent solution. After assimilating radial velocity, the simulated reflectivity (Figure 2d–f) was also improved. Compared with the improvements made by assimilating reflectivity (Figure 2a–c), the improvements made by assimilating radial velocity (Figure 2d–f)) were much smaller. This may be because assimilating reflectivity has a direct impact on the simulated reflectivity, but assimilating radial velocity can only impact the simulated reflectivity indirectly through cross-covariance. Unlike the improvement made when assimilating reflectivity, the further improvement was much smaller when the iterations were increased when assimilating radial velocity. As shown in Figures 2d–f), the improvements made in NLS1-V, NLS2-V, and NLS3-V were almost the same. This may be because the radial velocity observation operator is linear, while the reflectivity observation operator is non-linear; the nonlinearity impact was weaker when assimilating radial velocity than when assimilating reflectivity. According to the theory of NRAS, the advantages of NRAS over PRAS are fewer when assimilating radial velocity than when assimilating reflectivity.

Furthermore, the root-mean-square errors (RMSEs) at the time of analysis for six basic model variables were compared, as shown in Table 1. After assimilating either reflectivity or radial velocity with NRAS, compared with the CTL experiment, the RMSEs for all variables gradually decreased when the iterations increased, the decreasing amplitude became smaller when the iterations were increased. This result indicated that NRAS outperformed PRAS in assimilating the radar data. It was also found that assimilating reflectivity led to a larger improvement in the vertical velocity, the perturbation potential temperature, the water vapor mixing ratio, and the rainwater mixing ratio than the assimilating radial velocity, while assimilating radial velocity led to a larger improvement in the zonal wind, meridional wind, and perturbation pressure than assimilating reflectivity, which indicated that

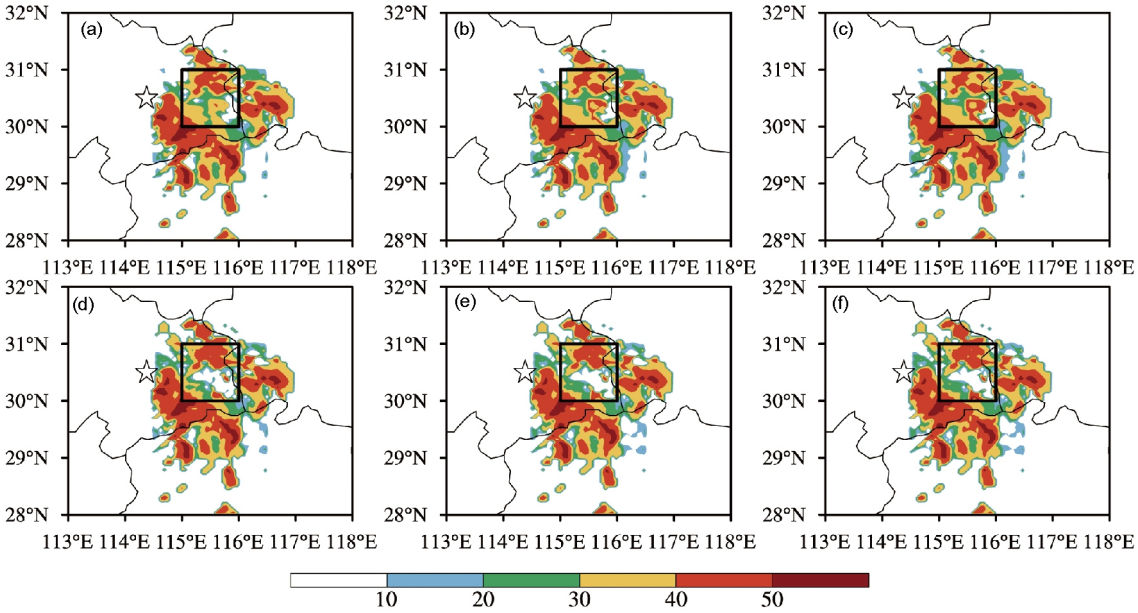

Figure 2 The radar reflectivity (dBZ) at the eighth model level at the time of analysis for (a) NLS1-R, (b) NLS2-R, (c) NLS3-R, (d) NLS1-V, (e) NLS2-V, and (f) NLS3-V. The black star represents the location of the Doppler radar in Wuhan.

Table 1 The RMSEs for *U*, *V*, *W*, *T*, *P*, *QV*, and *QR* at the time of analysis for the CTL, NLS1-R, NLS2-R, NLS3-R, NLS1-V, NLS2-V, and NLS3-V experiments[a)]

	U (m s^{-1})	*V* (m s^{-1})	*W* (m s^{-1})	*T* (K)	*P* (Pa)	*QV* (g kg^{-1})	*QR* (g kg^{-1})
CTL	3.000	3.127	0.397	1.418	40.139	0. 671	0. 257
NLS1-R	2.943	3.060	0.379	1.401	39.965	0. 659	0. 238
NLS2-R	2.916	3.038	0.373	1.394	39.803	0. 653	0. 231
NLS3-R	2.909	3.032	0.371	1.393	39.758	0. 652	0. 230
NLS1-V	2.917	3.042	0.380	1.403	39.613	0. 663	0. 244
NLS2-V	2.885	3.011	0.376	1.398	39.345	0. 659	0. 240
NLS3-V	2.877	3.003	0.374	1.396	39.264	0. 658	0. 239

a) *U*, zonal wind; *V*, meridional wind; *W*, vertical velocity; *T*, perturbation potential temperature; *P*, perturbation pressure; *QV*, water vapor mixing ratio; *QR*, rainwater mixing ratio

the two types of radar data have different impacts on different variables.

The RMSEs in the vertical direction for four model variables (zonal wind, meridional wind, vertical velocity, and rainwater-mixing ratio) were further compared in Figures 3 and 4 to evaluate NRAS against PRAS. After assimilating either reflectivity or radial velocity (Figures 3 and 4), compared with the CTL experiment, NLS1-R and NLS1-V, NLS2-R and NLS2-V, and NLS3-R and NLS3-V all reduced the RMSEs at most model layers. NLS2-R (NLS2-V) further reduced the RMSEs over NLS1-R (NLS1-V). When NLS3-R (NLS3-V) was compared with NLS2-R (NLS2-V), the RMSEs were further decreased. This result also demonstrated that NRAS could make further improvements with more iterations compared with PRAS. The decreasing amplitude became smaller in NLS3-R (NLS3-V), which indicated that a limited number of iterations (two iterations in this study) can yield a convergent result. When comparing the improvement made by assimilating reflectivity with that by assimilating radial velocity (Figures 3 and 4), the largest difference was found in the rainwater mixing ratio, with the difference mainly occurring in the lower layers. Assimilating reflectivity led to a larger improvement in the rainwater mixing ratio than assimilating radial velocity, which was consistent with the results shown in Table 1. According to the reflectivity observation operator (eq. (7)), reflectivity is directly related to the rainwater mixing ratio; thus, assimilating reflectivity naturally can lead to larger improvements in the rainwater mixing ratio than assimilating radial velocity.

In summary, NRAS with iterations greater than one outperformed PRAS in improving initial condition. When increasing the iterations, the NRAS can gradually improve initial condition. These improvements will become fewer with increased iterations, and a limited number of iterations can yield a convergent result. Because the observation operators for reflectivity and radial velocity are nonlinear and linear, respectively, the nonlinearity impacts will be stronger when assimilating reflectivity. Therefore, by increasing the iterations, the improvements made when assimilating reflectivity were larger than those made when assimilating radial velocity. In addition, assimilating reflectivity and radial velocity had different impacts on model variables. In particular, because reflectivity is directly related to the rainwater mixing ratio, assimilating reflectivity led to larger improvements in the rainwater mixing ratio than assimilating radial velocity.

3.3 Results of the forecasts

To comprehensively evaluate the performance of the NRAS

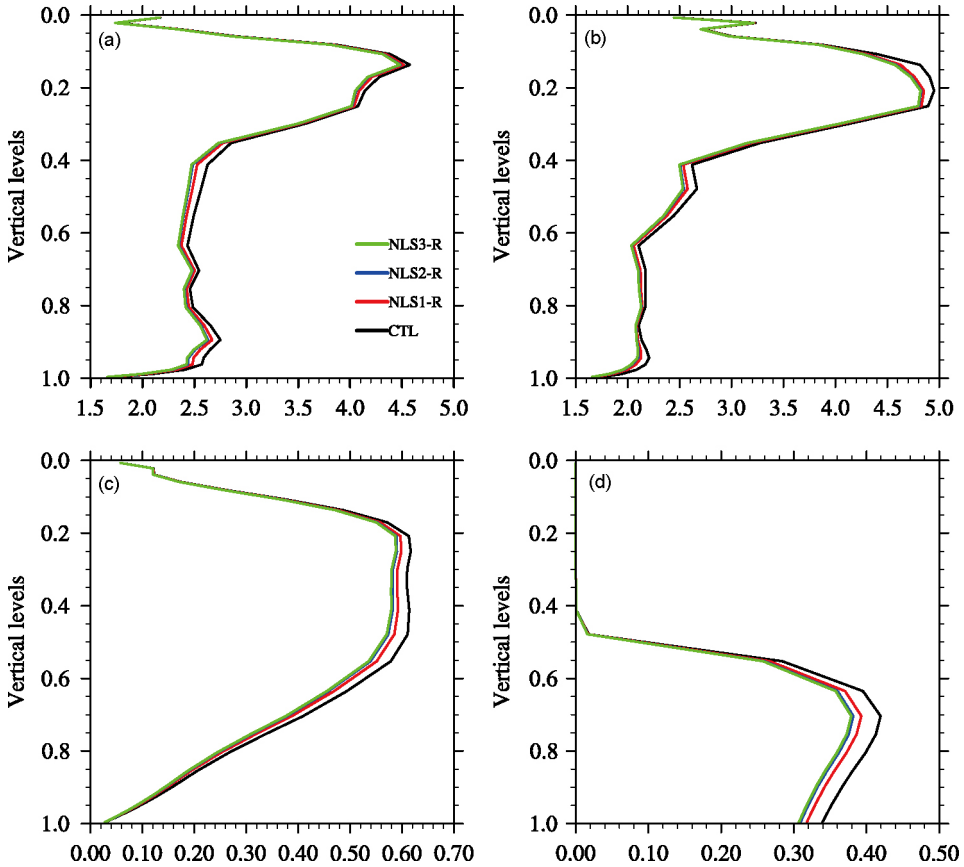

Figure 3 The vertical profiles of the RMSEs in (a) zonal wind (m s^{-1}), (b) meridional wind (m s^{-1}), (c) vertical velocity (m s^{-1}), and (d) rainwater-mixing ratio (g kg^{-1}) from the CTL, NLS1-R, NLS2-R, and NLS3-R at the time of analysis.

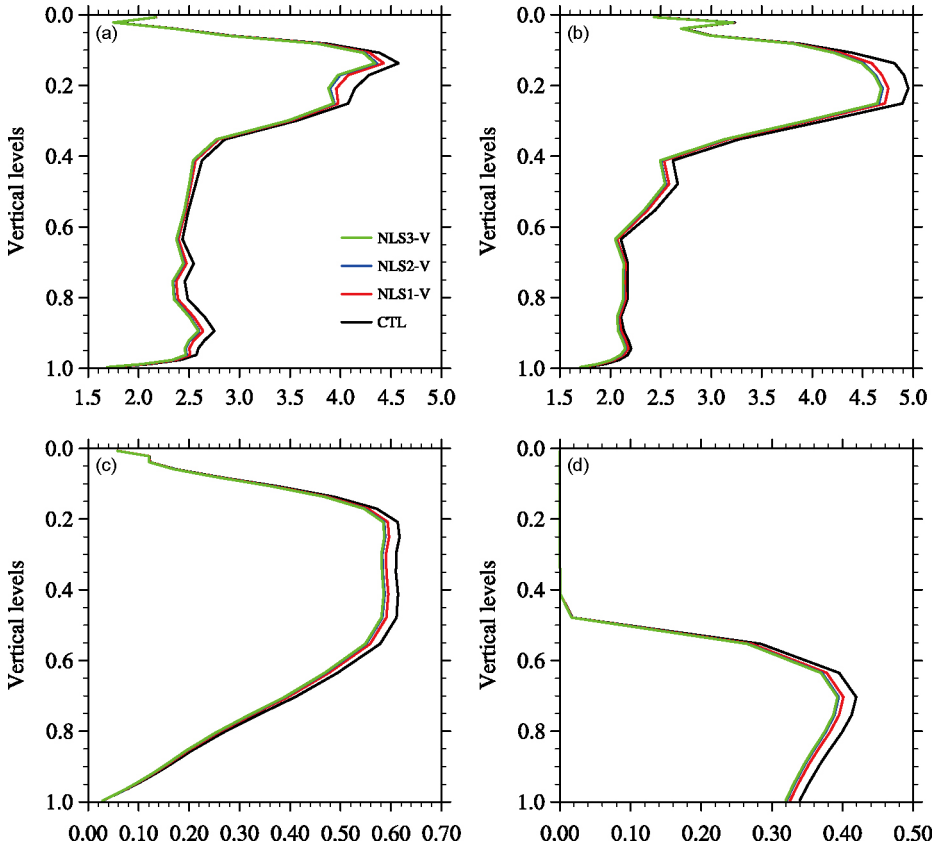

Figure 4 The vertical profiles of the RMSEs in (a) zonal wind (m s^{-1}), (b) meridional wind (m s^{-1}), (c) vertical velocity (m s^{-1}), and (d) rainwater-mixing ratio (g kg^{-1}) from the CTL, NLS1-V, NLS2-V, and NLS3-V at the time of analysis.

against the PRAS, the forecasts for four model variables (zonal wind, meridional wind, vertical velocity, and rainwater-mixing ratio) and hourly accumulated rainfall were further investigated.

Figure 5 shows the RMSEs of the four model variables for a 6-hour forecast. The RMSEs were decreased in the assimilation window (from 00UTC to 01UTC, 00UTC indicates the time of analysis), which demonstrated that NRAS could effectively assimilate radar data. After assimilating either reflectivity or radial velocity by NRAS, for the zonal and meridional wind, the RMSEs of the 6-hour forecast were smaller than those in the CTL experiment, which demonstrated that NRAS could effectively improve the forecast. The RMSEs of the forecast gradually decreased as the iterations were increased, with two iterations yielding a convergent result, which was consistent with improvement in the initial condition (Figure 5a–d). This result indicates that the NRAS outperformed the PRAS in improving the forecast. For the zonal and meridional wind, assimilating radial velocity led to a larger improvement than assimilating reflectivity, especially in the later period of the 6-hour forecast. For the vertical velocity and the rainwater mixing ratio (Figure 5e–h), assimilating reflectivity only contributed to improvements in the first 2 hours of the forecast. In contrast, assimilating radial velocity made improvements in the first 5 hours of the forecast; although the improvements were small, they lasted longer. However, in the first 2 hours of the forecast, the improvements made by assimilating reflectivity were larger than those made by assimilating radial velocity, especially for the rainwater mixing ratio.

Assimilating radar data can improve rainfall forecasts (Wang S Z et al., 2013; Sun and Wang, 2013). The improvement of rainfall forecasts was investigated to further evaluate NRAS against PRAS. The RMSEs of the hourly accumulated rainfall forecast are shown in Figure 6. It can be seen that compared with CTL (black line), after assimilating reflectivity, the hourly accumulated rainfall was improved in about the first 2-hour forecast (Figure 6a), and after assimilating radial velocity, the hourly accumulated rainfall was improved in the first 5-hour forecast (Figure 6b). The rainfall process depends on many model variables (e.g., wind, temperature, and rainwater mixing ratio) through model dynamics and thermodynamics (Tian and Feng, 2015). As shown in Figure 5, the zonal and meridional winds were improved in the 6-hour forecast after assimilating either reflectivity or radial velocity, while for the vertical velocity and rainwater mixing ratio, the improvement only lasted from 00UTC to 02UTC after assimilating reflectivity, and from 00UTC to 05UTC after assimilating radial velocity. In contrast to the improvement for the 6-hour forecast of the hourly accumulated

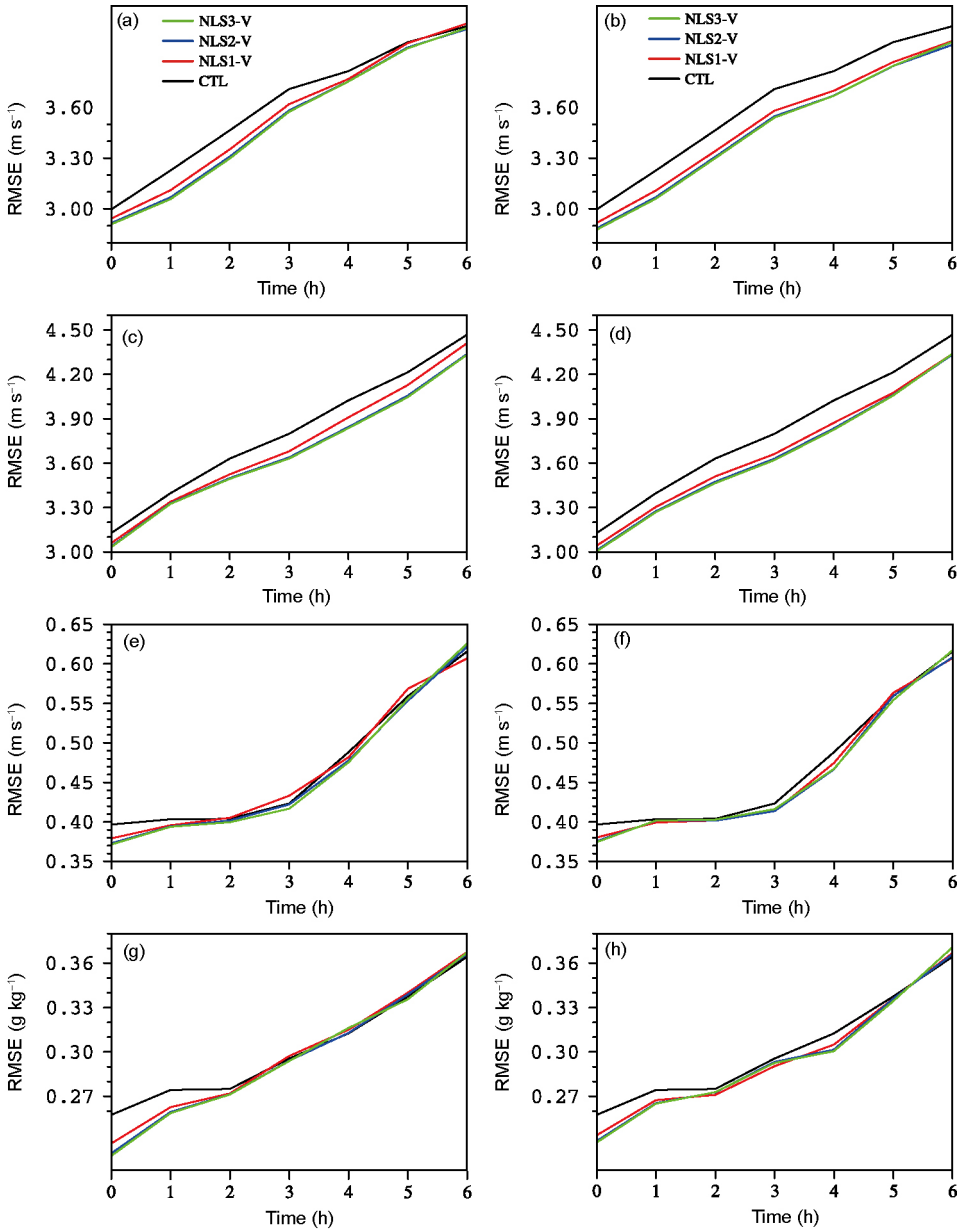

Figure 5 The RMSEs of the 6-hour forecast for zonal wind: (a) and (b), meridional wind: (c) and (d), vertical velocity: (e) and (f), and rainwater-mixing ratio: (g) and (h). The left panel and right panel represent the results of assimilating reflectivity and assimilating radial velocity, respectively. The "0" on the *x*-axis indicates the time of analysis.

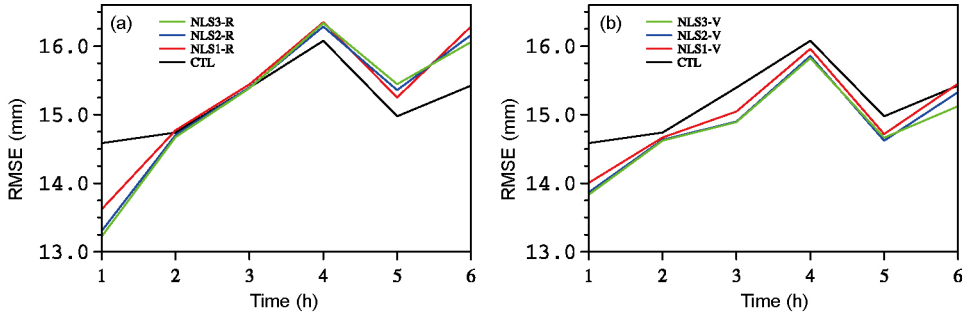

Figure 6 The RMSEs of the 6-hour forecast for the hourly accumulated rainfall forecast after (a) assimilating reflectivity and (b) assimilating radial velocity. The black line, red line, blue line, and green line indicate the CTL, NLS1-R (NLS1-V), NLS2-R (NLS2-V), and NLS3-R (NLS3-V), respectively. The "1" on the *x*-axis means 1 hour after the time of analysis.

rainfall (Figure 6), the vertical velocity and rainwater mixing ratio corresponded well to the hourly accumulated rainfall forecast. Furthermore, the magnitude of improvement for the vertical velocity and rainwater mixing ratio also corresponded well to the magnitude of improvement for the hourly accumulated rainfall forecast, and thus the above results indicate that among the basic variables, the forecast of vertical velocity and rainwater mixing ratio can well reflect the forecast of rainfall. Because assimilating reflectivity led to larger improvements in the vertical velocity and rainwater mixing ratio than assimilating radial velocity in the first 2-hour forecast (Figure 5), a larger improvement in the hourly accumulated rainfall forecast was obtained by assimilating reflectivity (Figure 6). However, without the retrieved buoyancy and the resulting updraft, the rainwater obtained by the assimilation of reflectivity can fall to the ground quickly (Sun and Wang, 2013). Although assimilating reflectivity led to a larger improvement in the hourly accumulated rainfall forecast in the early stages (Figure 6a), the improvement was not observed in the following stage due to the worse analysis of the vertical velocity and rainwater mixing ratio in this stage. Because assimilating radial velocity led to a sustained improvement in the vertical velocity and rainwater mixing ratio for a longer time, the hourly accumulated rainfall forecast correspondingly improved for a longer time (Figure 6b).

In general, the NRAS outperformed the PRAS in assimilating radar data and improving the rainfall forecast. Similar to the above results, NRAS with two iterations yielded a convergent result. The largest improvement in the hourly accumulated rainfall occurred in the first hour of the forecast. The absolute errors of the hourly accumulated rainfall in the first hour of the forecast are shown in Figure 7. Compared with CTL (Figure 7a), after assimilating either reflectivity or radial velocity, the absolute errors (Figure 7b–g) were gradually decreased by increasing the iterations. However, the differences (Figure 7e–g) among NLS1-V, NLS2-V, and NLS3-V were much smaller than those (Figure 7b–d) among NLS1-R, NLS2-R, and NLS3-R, which indicated that, by increasing the iterations for NRAS, the further improvement made after assimilating radial velocity was much smaller than the improvement made after assimilating reflectivity. This may be due to the nonlinear impact being larger when assimilating reflectivity. In addition, with the same iterations for NRAS, assimilating reflectivity led to a larger improvement than assimilating radial velocity, but could be deduced by a better analysis of the vertical velocity and rainwater mixing ratio

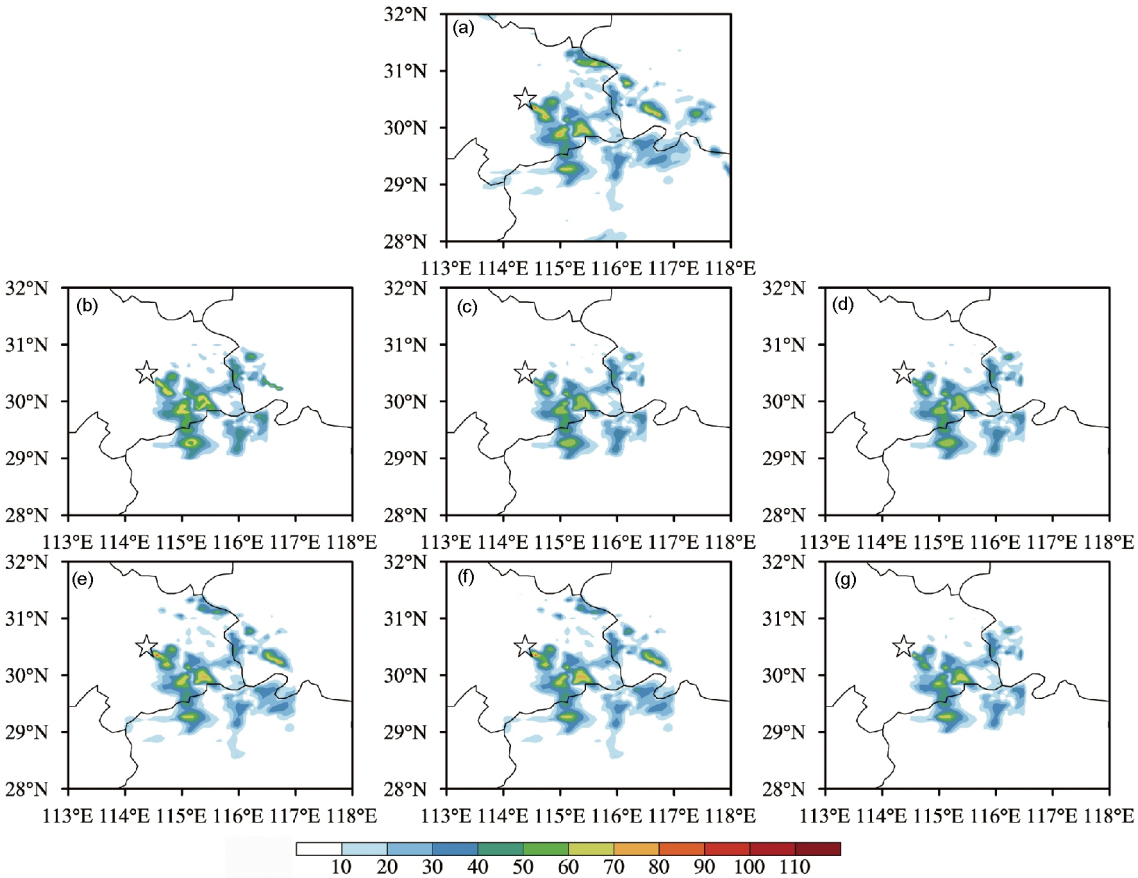

Figure 7 The absolute errors in the hourly accumulated rainfall (mm) in the first hour of the forecast for (a) CTL, (b) NLS1-R, (c) NLS2-R, (d) NLS3-R, (e) NLS1-V, (f) NLS2-V, and (g) NLS3-V. The black star represents the location of the Doppler radar in Wuhan.

after assimilating reflectivity in the early period (Figure 5e–h); the vertical velocity and rainwater mixing ratio corresponded well to the hourly accumulated rainfall forecast.

4. Summary

To enhance the capability of PRAS (Zhang et al., 2015) for effectively assimilating radar reflectivity and radial velocity, based on the proposed NLS-4DVar approach (Tian and Feng, 2015), PRAS was upgraded to a new radar data assimilation scheme, NRAS. The potential of NRAS compared to PRAS was investigated using OSSEs. Reflectivity and radial velocity were assimilated individually in the OSSEs, in which NRAS with one, two, and three iterations was conducted.

The results demonstrated that the NRAS could effectively assimilate radar data and gradually improved the initial condition by increasing the iterations, and the NRAS substantially outperformed PRAS in radar data assimilation. Further improvements became smaller as the iterations were increased, with a limited number of iterations yielding a convergent assimilation solution. By increasing the iterations for NRAS, the improvement made by assimilating reflectivity was larger than the improvement made by assimilating radial velocity. This can be explained by the fact that the reflectivity observation operator is nonlinear, while the radial velocity observation operator is linear, and therefore the nonlinear impact was larger when assimilating reflectivity. The advantage of the NRAS over PRAS is therefore obvious. In addition, assimilating reflectivity and radial velocity has different impacts on the model variables. Notably, because reflectivity is directly related to the rainwater mixing ratio, assimilating reflectivity led to a larger improvement in the rainwater mixing ratio.

To comprehensively investigate the potential of NRAS compared to PRAS, the forecasts for some model variables and hourly accumulated rainfall were evaluated. By increasing the iterations, the NRAS gradually improved the 6-hour forecast and almost outperformed the PRAS. Because the nonlinear impact was larger when assimilating reflectivity, the improvement made after assimilating radial velocity was much smaller than the improvement made after assimilating reflectivity when the iterations were increased. In contrast to the improvement in the forecast of the model variables, the vertical velocity and the rainwater mixing ratio corresponded well to the hourly accumulated rainfall forecast. Assimilating reflectivity led to a larger improvement in the forecast of the vertical velocity and rainwater mixing ratio in the early period, which led to a larger improvement in the hourly accumulated rainfall forecast. Assimilating radial velocity improved the forecast of the vertical velocity and rainwater mixing ratio for a longer time, which led to a longer improvement in the hourly accumulated rainfall forecast.

Acknowledgements *This work was partially supported by the National Key Research and Development Program of China (Grant No. 2016YFA0600203), the High-resolution Earth Observation System Major Special Project (CHEOS) (Grant No. 32-Y20A17-9001-15/17), the National Natural Science Foundation of China (Grant No. 41575100) and the Special Fund for Meteorological Scientific Research in Public Interest (Grant No. GYHY201306045).*

References

Aksoy A, Dowell D C, Snyder C. 2009. A multicase comparative assessment of the ensemble Kalman filter for assimilation of radar observations. Part I: Storm-scale analyses. Mon Weather Rev, 137: 1805–1824

Aksoy A, Dowell D C, Snyder C. 2010. A multicase comparative assessment of the ensemble Kalman filter for assimilation of radar observations. Part II: Short-range ensemble forecasts. Mon Weather Rev, 138: 1273–1292

Andersson E, Fisher M, Hólm E, Isaksen L, Radnóti G, Trémolet Y. 2005. Will the 4D-Var approach be defeated by nonlinearity? ECMWF Tech Memo

Beck A, Ehrendorfer M. 2005. Singular-vector-based covariance propagation in a quasigeostrophic assimilation system. Mon Weather Rev, 133: 1295–1310

Bocquet M, Sakov P. 2014. An iterative ensemble Kalman smoother. Q J R Meteorol Soc, 140: 1521–1535

Buehner M, Morneau J, Charette C. 2013. Four-dimensional ensemble-variational data assimilation for global deterministic weather prediction. Nonlinear Process Geophys, 20: 669–682

Caya A, Sun J, Snyder C. 2005. A comparison between the 4DVAR and the ensemble Kalman filter techniques for radar data assimilation. Mon Weather Rev, 133: 3081–3094

Cheng H, Jardak M, Alexe M, Sandu A. 2010. A hybrid approach to estimating error covariances in variational data assimilation. Tellus A, 62: 288–297

Choi Y, Lim G H, Lee D K. 2013. Radar radial wind data assimilation using the time-incremental 4D-Var method implemented to the WRFDA system. Tellus A, 65: 19677

Courtier P, Thépaut J N, Hollingsworth A. 1994. A strategy for operational implementation of 4D-Var, using an incremental approach. Q J R Meteorol Soc, 120: 1367–1387

Courtier P. 2007. Dual formulation of four-dimensional variational assimilation. Q J R Meteorol Soc, 123: 2449–2461

Desroziers G, Camino J T, Berre L. 2014. 4DEnVar: Link with 4D state formulation of variational assimilation and different possible implementations. Q J R Meteorol Soc, 140: 2097–2110

Dowell D C, Zhang F, Wicker L J, Snyder C, Crook N A. 2004. Wind and temperature retrievals in the 17 May 1981 Arcadia, Oklahoma, supercell: Ensemble Kalman filter experiments. Mon Weather Rev, 132: 1982–2005

Evensen G. 1994. Sequential data assimilation with a nonlinear quasi-geostrophic model using Monte Carlo methods to forecast error statistics. J Geophys Res, 99: 10143

Evensen G. 2003. The ensemble Kalman filter: Theoretical formulation and practical implementation. Ocean Dyn, 53: 343–367

Evensen G. 2004. Sampling strategies and square root analysis schemes for the EnKF. Ocean Dyn, 54: 539–560

Fairbairn D, Pring S R, Lorenc A C, Roulstone I. 2014. A comparison of 4DVar with ensemble data assimilation methods. Q J R Meteorol Soc, 140: 281–294

Gao J, Xue M, Brewster K, Droegemeier K K. 2004. A three-dimensional variational data analysis method with recursive filter for Doppler radars. J Atmos Ocean Technol, 21: 457–469

Gaspari G, Cohn S E. 1999. Construction of correlation functions in two and three dimensions. Q J R Meteorol Soc, 125: 723–757

Hu M, Xue M, Brewster K. 2006a. 3DVAR and cloud analysis with WSR-88D Level-II data for the prediction of the Fort Worth, Texas, tornadic thunderstorms. Part I: Cloud analysis and its impact. Mon Weather Rev,

134: 675–698
Hu M, Xue M, Gao J, Brewster K. 2006b. 3DVAR and cloud analysis with WSR-88D Level-II data for the prediction of the Fort Worth, Texas, Tornadic thunderstorms. Part II: Impact of radial velocity analysis via 3DVAR. Mon Weather Rev, 134: 699–721
Huang X Y, Xiao Q, Barker D M, Zhang X, Michalakes J, Huang W, Henderson T, Bray J, Chen Y, Ma Z, Dudhia J, Guo Y, Zhang X, Won D J, Lin H C, Kuo Y H. 2009. Four-dimensional variational data assimilation for WRF: Formulation and preliminary results. Mon Weather Rev, 137: 299–314
Jung Y, Zhang G, Xue M. 2008. Assimilation of simulated polarimetric radar data for a convective storm using the ensemble Kalman filter. Part I: Observation operators for reflectivity and polarimetric variables. Mon Weather Rev, 136: 2228–2245
Jung Y, Xue M, Zhang G. 2010. Simultaneous estimation of microphysical parameters and the atmospheric state using simulated polarimetric radar data and an ensemble Kalman filter in the presence of an observation operator error. Mon Weather Rev, 138: 539–562
Kain J S, Xue M, Coniglio M C, Weiss S J, Kong F, Jensen T L, Brown B G, Gao J, Brewster K, Thomas K W, Wang Y, Schwartz C S, Levit J J. 2010. Assessing advances in the assimilation of radar data and other mesoscale observations within a collaborative forecasting-research environment. Weather Forecast, 25: 1510–1521
Kalnay E, Yang S C. 2010. Accelerating the spin-up of ensemble Kalman Filtering. Q J R Meteorol Soc, 136: 1644–1651
. 2010. Kalnay E, Yang S C. 2008. Accelerating the spin-up of Ensemble Kalman Filtering. Q J R Meteorol Soc, 136: 1644–1651
Kawabata T, Seko H, Saito K, Kuroda T, Tamiya K, Tsuyuki T, Honda Y, Wakazuki Y. 2007. An assimilation and forecasting experiment of the nerima heavy rainfa11 with a cloud-resolving nonhydrostatic 4-dimensional variational data assimilation system. J Meteorol Soc Jpn, 85: 255–276
Kawabata T, Kuroda T, Seko H, Saito K. 2011. A cloud-resolving 4DVAR assimilation experiment for a local heavy rainfall event in the Tokyo metropolitan area. Mon Weather Rev, 139: 1911–1931
Kleist D T, Ide K. 2015a. An OSSE-based evaluation of hybrid variational-ensemble data assimilation for the NCEP GFS. Part I: System description and 3D-hybrid results. Mon Weather Rev, 143: 433–451
Kleist D T, Ide K. 2015b. An OSSE-based evaluation of hybrid variational-ensemble data assimilation for the NCEP GFS. Part II: 4DEnVar and hybrid variants. Mon Weather Rev, 143: 452–470
Liu C, Xiao Q, Wang B. 2008. An ensemble-based four-dimensional variational data assimilation scheme. Part I: Technical formulation and preliminary test. Mon Weather Rev, 136: 3363–3373
Liu C, Xiao Q, Wang B. 2009. An ensemble-based four-dimensional variational data assimilation scheme. Part II: Observing system simulation experiments with advanced research WRF (ARW). Mon Weather Rev, 137: 1687–1704
Lorenc A C. 2003. The potential of the ensemble Kalman filter for NWP—A comparison with 4D-Var. Q J R Meteorol Soc, 129: 3183–3203
Lorenc A C. 2013. Recommended nomenclature for EnVar data assimilation methods. Research Activities in Atmospheric and Oceanic Modeling. WGNE, 2 URL: http://www.wcrp-climate.org/WGNE/BlueBook/2013/individual-articles/01_Lorenc_Andrew_EnVar_nomenclature.pdf
Lorenc A C, Bowler N E, Clayton A M, Pring S R, Fairbairn D. 2015. Comparison of hybrid-4DEnVar and hybrid-4DVar Data assimilation methods for global NWP. Mon Weather Rev, 143: 212–229
Munsell E B, Zhang F. 2014. Prediction and uncertainty of Hurricane Sandy (2012) explored through a real-time cloud-permitting ensemble analysis and forecast system assimilating airborne Doppler radar observations. J Adv Model Earth Syst, 6: 38–58
Parrish D F, Derber J C. 1992. The national meteorological cente's spectral statistical-interpolation analysis system. Mon Weather Rev, 120: 1747–1763
Poterjoy J, Zhang F. 2015. Systematic comparison of Four-Dimensional data assimilation methods with and without the tangent linear model using hybrid background error covariance: E4DVar versus 4DEnVar. Mon Weather Rev, 143: 1601–1621
Qiu C, Shao A, Xu Q, Wei L. 2007. Fitting model fields to observations by using singular value decomposition: An ensemble-based 4DVar approach. J Geophys Res, 112: D11105
Sakov P, Oliver D S, Bertino L. 2012. An iterative EnKF for strongly nonlinear systems. Mon Weather Rev, 140: 1988–2004
Snook N, Xue M, Jung Y. 2011. Analysis of a tornadic mesoscale convective vortex based on ensemble Kalman filter assimilation of CASA X-Band and WSR-88D radar data. Mon Weather Rev, 139: 3446–3468
Snyder C, Zhang F. 2003. Assimilation of simulated doppler radar observations with an ensemble Kalman filter. Mon Weather Rev, 131: 1663–1677
Sugimoto S, Crook N A, Sun J, Xiao Q, Barker D M. 2009. An examination of WRF 3DVAR radar data assimilation on its capability in retrieving unobserved variables and forecasting precipitation through observing system simulation experiments. Mon Weather Rev, 137: 4011–4029
Sun J, Crook N A. 1997. Dynamical and microphysical retrieval from Doppler radar observations using a cloud model and its adjoint: Part I. Model development and simulated data experiments. J Atmos Sci, 54: 1642–1661
Sun J, Crook N A. 1998. Dynamical and microphysical retrieval from Doppler radar observations using a cloud model and its adjoint: Part II. Retrieval experiments of an observed Florida convective storm. J Atmos Sci, 55: 835–852
Sun J, Wang H. 2013. Radar data assimilation with WRF 4D-Var. Part II: Comparison with 3D-Var for a squall line over the U.S. Great Plains. Mon Weather Rev, 141: 2245–2264
Tong M, Xue M. 2005. Ensemble Kalman filter assimilation of Doppler radar data with a compressible nonhydrostatic model: OSS experiments. Mon Weather Rev, 133: 1789–1807
Tian X, Xie Z, Dai A. 2008. An ensemble-based explicit four-dimensional variational assimilation method. J Geophys Res, 113: D21124
Tian X, Xie Z, Sun Q. 2011. A POD-based ensemble four-dimensional variational assimilation method. Tellus A, 63: 805–816
Tian X, Xie Z, Liu Y, Cai Z, Fu Y, Zhang H, Feng L. 2014. A joint data assimilation system (Tan-Tracker) to simultaneously estimate surface CO_2 fluxes and 3-D atmospheric CO_2 concentrations from observations. Atmos Chem Phys, 14: 13281–13293
Tian X, Feng X. 2015. A non-linear least squares enhanced POD-4DVar algorithm for data assimilation. Tellus A, 67: 25340
Wang B, Liu J, Wang S, Cheng W, Juan L, Liu C, Xiao Q, Kuo Y H. 2010. An economical approach to four-dimensional variational data assimilation. Adv Atmos Sci, 27: 715–727
Wang H L, Auligné T, Morrison H. 2012. Impact of microphysics scheme complexity on the propagation of initial perturbations. Mon Weather Rev, 140: 2287–2296
Wang H L, Sun J Z, Fan S Y, Huang X Y. 2013a. Indirect assimilation of radar reflectivity with WRF 3D-Var and its impact on prediction of four summertime convective events. J Appl Meteorol Climatol, 52: 889–902
Wang H L, Sun J Z, Zhang X, Huang X Y, Auligné T. 2013b. Radar data assimilation with WRF 4D-Var. Part I: System development and preliminary testing. Mon Weather Rev, 141: 2224–2244
Wang S Z, Xue M, Schenkman A D, Min J Z. 2013. An iterative ensemble square root filter and tests with simulated radar data for storm-scale data assimilation. Q J R Meteorol Soc, 139: 1888–1903
Wang X G, Barker D M, Snyder C, Hamill T M. 2008. A hybrid ETKF-3DVAR data assimilation scheme for the WRF Model. Part I: Observing system simulation experiment. Mon Weather Rev, 136: 5116–5131
Weng Y H, Zhang M, Zhang F Q. 2011. Advanced data assimilation for cloud-resolving hurricane initialization and prediction. Comput Sci Eng,

13: 40–49
Weng Y H, Zhang F Q. 2012. Assimilating airborne Doppler Radar observations with an ensemble Kalman filter for convection-permitting hurricane initialization and prediction: Katrina (2005). Mon Weather Rev, 140: 841–859
Xiao Q, Kuo Y H, Sun J, Lee W C, Lim E, Guo Y R, Barker D M. 2005. Assimilation of Doppler radar observations with a regional 3DVAR system: Impact of Doppler velocities on forecasts of a heavy rainfall case. J Appl Meteorol, 44: 768–788
Xiao Q, Kuo Y H, Sun J, Lee W C, Barker D M, Lim E. 2007. An approach of radar reflectivity data assimilation and its assessment with the inland QPF of Typhoon Rusa (2002) at Landfall. J Appl Meteorol Climatol, 46: 14–22
Xiao Q, Sun J. 2007. Multiple-Radar data assimilation and short-range quantitative precipitation forecasting of a squall line observed during IHOP_2002. Mon Weather Rev, 135: 3381–3404
Xiao Q, Sun J, Lee W C, Kuo Y H, Barker D M, Lim E, Won D J, Lee M S, Lee W J, Cho J Y, Lee D K, Lee H S. 2008. Doppler radar data assimilation in KMA's operational forecasting. Bull Amer Meteorol Soc, 89: 39–43
Xue M, Kong F Y, Thomas K W, Wang Y F, Brewster K, Gao J D, Wang X G, Weiss S, Clark A, Kain J, Coniglio M, Du J, Jensen T, Kuo Y H. 2010. CAPS realtime storm scale ensemble and high resolution forecast for the NOAA Hazardous Weather Testbed 2010 Spring Experiment. In: 25th Conferences Severe Local Storms. Denver
Yang S C, Kalnay E, Hunt B. 2012. Handling nonlinearity in an ensemble Kalman filter: Experiments with the Three-variable lorenz model. Mon Weather Rev, 140: 2628–2646
Zhang B, Tian X, Sun J, Chen F, Zhang Y, Zhang L, Fu S. 2015. PO-DEn4DVar-based radar data assimilation scheme: Formulation and preliminary results from real-data experiments with advanced research WRF (ARW). Tellus A, 67: 26045
Zhang F. 2011. The future of hurricane prediction. Comput Sci Eng, 13: 9–12
Zhang F, Weng Y, Gamache J F, Marks F D. 2011. Performance of convection-permitting hurricane initialization and prediction during 2008–2010 with ensemble data assimilation of inner-core airborne Doppler radar observations. Geophys Res Lett, 38: L15810